# MINIPANDA – A SMALL-SCALE CONTAINMENT TEST FACILITY WITH NOVEL INSTRUMENTATION IS USED FOR CODE VALIDATION FOR AN AIR INGRESS SCENARIO

M. Ritterath<sup>1</sup>, J. Baggemann<sup>2</sup>, S. Kelm<sup>2</sup>, O. C. Öztürk<sup>1</sup> and H.-M. Prasser<sup>1</sup>

Swiss Federal Institute of Technology (ETH), Zurich, Switzerland

Forschungszentrum Jülich GmbH (FZJ), Jülich, Germany

Martinri@ethz.ch, s.kelm@fz-juelich.de

#### **Abstract**

"MiniPanda", a small-scale containment test facility built at ETH Zürich, was equipped with novel field measurement techniques. The capabilities of the facility were demonstrated in a first test series on an air ingress scenario. The ingress of air into a helium cooled reactor is considered to be one of the most severe accidents for the GenIV-type helium cooled reactor. The air once arrived inside the reactor can cause the oxidation of the graphite structures.

The ingress of air into a helium environment was investigated experimentally and analytically using the commercial CFX-13 and StarCCM+ 5.06 CFD codes. The experimental volume consists of two cylindrical vessels that are filled separately with air or helium. The experiment is initiated by removing the blockage from the pipe connecting the two vessels. The experimental and analytical results of the consequent buoyancy-driven air ingress are compared against each other.

## 1. Introduction

Computational Fluid Dynamics (CFD) is used more and more widely in nuclear reactor safety, also for containment safety research. It is supposed to resolve issues which are of 3D character such as mixing processes that cannot be considered in an integrated manner, i.e. lumped over a large control volume (Smith 2008). CFD is well approved for many industrial flows such as flow over a wing and other forced convective flows. In contrary, for nuclear safety issues where the flow is often buoyancy driven, few experience on the quality of flow predictions is available. Therefore, extensive validation is necessary before CFD results can be accepted for safety relevant cases in design and evaluation (Teschendorff 2008). In the frame of containment analysis, the issues under attention are especially slow internal flows in large volumes, density driven flows and stratifications (Allelein, Fischer et al. 2007; NEA/CSNI 2008). This implies that further validation and extension of the existing models as well as development of new dedicated models for nuclear applications are necessary.

For validation purposes the large existing database of experiments, performed in large-scale integral test facilities, e.g. PANDA (PSI, Villigen, Switzerland), THAI (Becker Technologies, Eschborn, Germany) or MISTRA (CEA, Saclay, France) can be employed.

However, model development is performed on a scale which cannot be resolved in total by the instrumentation in large-scale integral test facilities, i.e. for model development small facilities with dense instrumentation are more suitable since 2 or even 3D measurements are preferred for CFD validation. In order to identify gaps in a model it is also important to focus the experiment

on a single phenomenon and to perform broad parametric variations in order to address for example different flow regimes and their transition phenomena.

To meet the experimental needs for CFD development, i.e. high resolution in space and time as well as availability of field data, small/medium (smart-)scale test facilities provide advantages over large-scale facilities. From the experimental side, small-scale experiments are much cheaper, easier to conduct and novel instrumentation can be installed. From the analytical side, small-scale experiments allow for mesh and parameter studies which would be unaffordable concerning the computational expenses. The method CFD is, in contrast to lumped parameter (LP) codes, scalable (correct meshing provided) because the governing equations don't contain reference length scales. Remaining empirical model constants (e.g., turbulence model) have been derived from experiments and by this contain information on their scale. But in contrary to the LP codes, empirical closure laws models for CFD are defined on the level of the calculation grid, and thus independent from the global geometry. Due to this fact, small-scale experiments are an important basis for model development, and play a complementary role to large-scale integral experiments in the validation scheme.

## 2. MiniPanda

MiniPanda is such a small (smart-) scale test facility, dedicated to the experimental investigation of phenomena that are relevant for the safety of nuclear reactor containments.

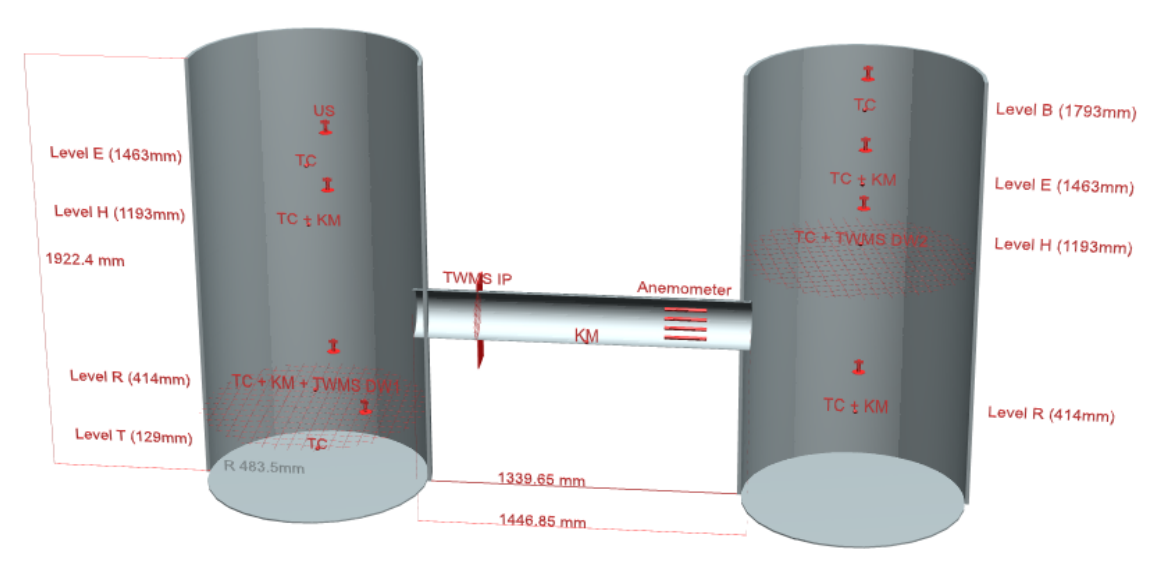
## 2.1 Scaling and geometrical specifications

MiniPanda has got its name from the fact that it is a 1:4 scaled down model of two out of four containment volumes of the large-scale, multi compartment nuclear reactor containment test facility PANDA (Dreier, Paladino et al. 2008) at Paul Scherrer Institute, Villigen, Switzerland. The small test facility was built at the Swiss Federal Institute of Technology (ETH) in Zurich. MiniPanda, see Figure 1, consists of two vessels (each 2 m high, 1 m diameter), that are interconnected by a horizontal pipe. The vessels are referred to as "Vessel 1" and "Vessel 2". The facility enables the application of advanced instrumentation, such as the in-house developed thermo-resistive mesh sensors that connect 520 temperature sensors in three planes. MiniPanda can be operated at ambient pressures and temperatures up to 100°C.

The vessels and the interconnecting pipe (IP) are made from PVC(-U). The vessel shells have a wall thickness of 16 mm, the vessel lid and bottom are 10 mm thick and the IP's wall thickness is 2.5 mm. The vessel wall thickness requires no further heat insulation, only the IP has been mantled with rubber foam blankets. For reasons of accessibility and manageability, each vessel is piled up from six segments. The IP consists of three flanged segments. Detailed geometrical information is available (Öztürk 2010).

## 2.2 Conventional instrumentation

The facility is equipped with thermocouples and katharometers to measure the helium molar fraction; both located on the vessel axes (see Figure 1). The helium molar fraction is computed also from an ultrasound time of flight measurement (Ritterath, Prasser et al. 2010) along the diameter of the vessel in four levels of each vessel. Four in-house developed anemometers (Ritterath, Voser et al. 2009) are placed above each other in the interconnecting pipe. Inside and outside wall thermocouples for both vessels allow for well controlled boundary conditions.



TC=thermocouple, KM=katharometer, TWMS=temperature mesh sensor.

## 2.3 The novel temperature mesh sensor

Wire-mesh sensors, as introduced by Prasser (Prasser, Böttger et al. 1998), are based on the detection of the local electrical conductivity of a fluid using grids of crossing electrode wires. The information about the local conductivity is obtained by supplying the electrode wires of the first grid (transmitter wires) with voltage pulses in a successive order. At the same time, the current arriving at the electrodes wires of the second grid (receiver wires), which are crossing the wires of the first grid in a small distance, is sampled. Wire-mesh sensors are used to measure phase distributions in gas-liquid flows with high time resolution, which allows the detailed characterization of the dynamic gas-liquid interface (Prasser 2007). A second field of application is mixing studies, where one of the involved fluids is labeled with a salt tracer affecting the conductivity (Kliem, Höhne et al.). A third application is high speed liquid film thickness measurement (Damsohn and Prasser 2009). If the electrodes are arranged flush to the wall the conductivity between the electrodes is defined by the thickness of the liquid film covering them. The wire-mesh electronic unit performs a measurement of the conductance matrix of the twodimensional network of resistive elements, usually formed by the conducting fluid being in contact with the transmitter and the receiver wire at each crossing point of the sensor matrix. A gas temperature distribution measurement can be realized by connecting transmitter and receiver wires via thermo-resistive elements arranged at the crossing points, which substitute the conducting fluid of the classical application case. This simple solution allows using standard signal acquisition units for wire-mesh sensors, provided thermo-resistive elements of a convenient conductance range are available.

Suitable thermo-resistive elements are negative or positive temperature coefficient semiconductors called thermistors, or any kind of metal resistors (Ritterath, Hampel et al. 2008 DE 10 2007 019 925 A1). Da Silva (Silva, Schleicher et al. 2009) described the application of Pt1000 resistors with a wire-mesh electronics unit. Disadvantageous in this case is the low resistance change due to temperature and consequently the low temperature resolution after sampling and discretisation. Instead the large resistance changes of a negative temperature

coefficient thermistor provide good resolution with the present device WMS-200 (teletronic 2007). Consequently, it is more convenient to use semiconductor thermistors.

A thermistor type with a reference resistance of 50 k $\Omega$  at 25°C with a resistance of 12.3 k $\Omega$  at 60°C was chosen. Eq. 1 approximates the transfer function of the thermistor around a reference temperature  $\theta_0$ .

$$22 = 20 \cdot \exp(212 - 120)$$
 (EPCOS 2009) (1)

where  $\theta$  is temperature,  $R_0$  is the reference resistance at  $\theta_0$ , the reference temperature and B the steepness coefficient. The nonlinear thermistor transfer function that connects temperature and resistance as well as the lower initial precision requires an adequate calibration function.

For each thermistor, a 3<sup>rd</sup> order calibration function (Eq. 2) is obtained by using the least square method to fit a curve into the calibration points. The calibration function type is derived by inserting Eq. 1 into the conductance transfer function of the wire-mesh acquisition unit and solving for the temperature. The higher order terms compensate for the approximate character of Eq. 1, being valid only for a limited temperature range around the reference temperature and thus allow for application of the calibration function for a wide temperature range (Öztürk 2010).

$$2??? = 2 \cdot \log ??? + 2 \cdot \log ?? + 2 \cdot \log$$

where ADC is the conversion result from the wire-mesh electronics unit and a, b, c and d are the polynomial coefficients.

Uncertainty of reference instrument [K]	0.01
Standard deviation of measurement [K]	0.067
Quality of calibration function fit [K]	0.1
Estimated long term stability of thermistors (6 month operation) [K]	1.5

Table 1: Components of measurement uncertainty

Two different designs applied to the presented experiments were:

- TMS-IP: A small sensor for a pipe with a diameter of 220 mm consisted of a matrix of 8x8 crossing points with a spatial pitch of 24 mm. A double-sided printed circuit board (PCB) served as a frame for holding two grids of wires. The transmitting wires were fixed to the front side of the board, while the receivers were fixed to the back side. The axial distance of both wire planes was consequently equal to the thickness of the PCB, which was about 2 mm. The circular flow cross-section was cut out of the PCB, so that the wires were stretched over the free cross-section. They were fixed at the border by soldering them to conducting pads on the PCB. The wires of both planes crossed under an angle of 90 degree. At the crossing points, SMD thermistors in a 0603 housing were laser soldered between a transmitter and a receiver wire (EPCOS, B57321V2473H060), see (EPCOS 2009).
- TMS-DW: Two large diameter temperature mesh sensors were constructed to be mounted in the circular cross-section of the cylindrical vessels of MiniPanda. They consisted of a matrix of 16x16 sensing elements with a pitch of 57 mm. This time, the wires were directly attached to hooks that were fixed to the walls. Each sensor was mounted into a segment of a cylindrical PVC pipe of 968 mm inner diameter and 16 mm wall thickness. The vessels were finally composed of a number of such elements, including those with a

mesh sensor. Small springs generated a nearly constant tension in the wires, which was needed to allow for thermal dilatation due to the different thermal expansion coefficients of the vessel (PVC) and the wire materials (stainless steel), as well as to reduce the impact of vibrations during the construction. Slightest stretching of the wires would otherwise have immediately lead to plastic deformation (or even destruction) and to the loss of the tension needed for stretching them straight. The two wire planes were spanned with an axial distance of 40 mm. For these sensors, leaded glass encapsulated thermistors with 0.8 mm tip size were used. (EPCOS, B57540G0503H000).

For an application in MiniPanda, three thermo-resistive mesh sensors (TMS) were constructed, one TMS-IP and two TMS-DW. The sensor wires were contacted to the wire-mesh signal acquisition unit by flat ribbon cables at the outside of the vessel segments or, respectively, at the edge of the PCB of the small sensor.

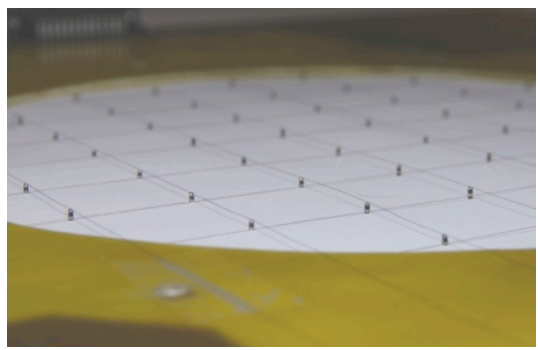


Figure 2: View on temperature mesh sensor, designed for the pipe.

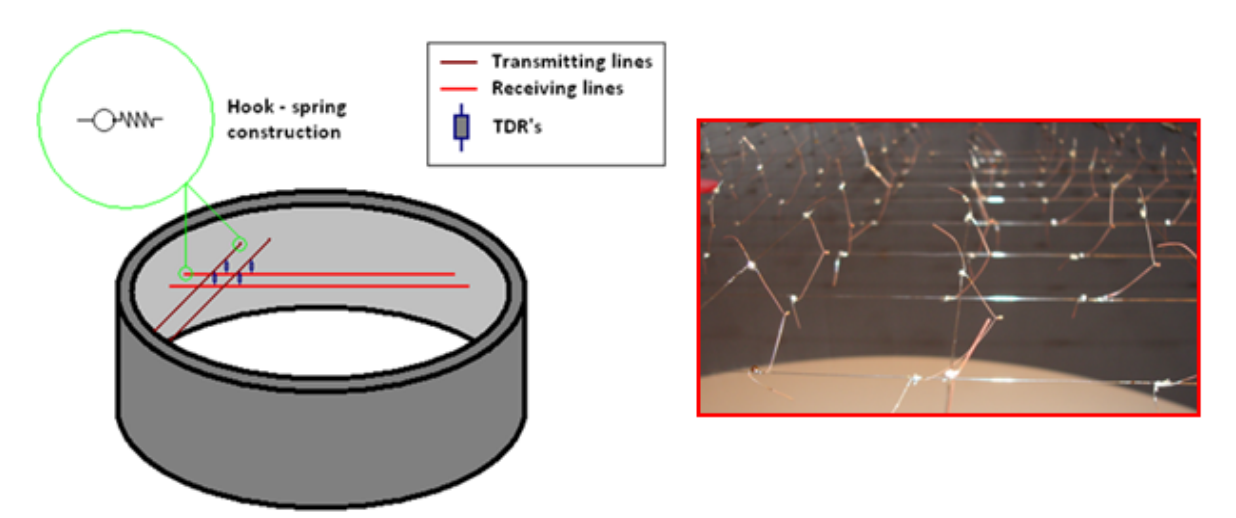


Figure 3: Construction principle of the temperature mesh sensor for the vessel cross sections (Melpignano and Vles 2009).

The main differences of the two thermistor types were their housing and consequently their mounting process and their dynamic behaviour. The glass encapsulated thermistors exhibited a response time of 0.8 s to a temperature jump induced by a hot jet. Their maximum operating temperature was 240°C. They were ideal for wire wrapping and for being soldered to large meshes with a receiver-transmitter layer distance between 40 and 70 mm. The SMD thermisitors exhibited a time constant of 1 s. They were designed for a maximum operation temperature of 125°C. They were well suited for PCB-mounting or for being soldered into small gaps, such as described for the small pipe mesh sensor.

Unfortunately, neither the glass case nore the SMD housing did seal the thermistors hermetically. Consequently, they could not be used in atmospheres with high humidity because water vapor destroys the sensing element. For the presented application, the thermoresistive mesh sensors were exclusively used for tests on the mixing of air and helium.

In the frame of the generic air ingress experiment described below, the facility was equipped with the already described three planes of temperature mesh sensors (see Figure 1): TMS-DW1 (horizontally) in the lower part of Vessel 1 where the hot air fell to the bottom, TMS-DW2 (horizontally) in Vessel 2 above the pipe entrance, where the cold helium rose and TMS-IP (vertically) in the pipe interconnecting both vessels.

## 3. Air Ingress

## 3.1 Test scenario

The very high temperature reactor (VHTR) is considered as a candidate for the Generation-IV reactor concepts. In contrast to the current light water reactors (LWR), the VHTR uses graphite as moderator and helium as coolant. The whole core structure, i.e. bottom, top and side reflectors as well as the fuel elements consist of- or contain graphite. The heat exchanger is placed under the core altitude so that in contrast to LWRs the coolant ducts are connected at the bottom part of the reactor. Usually the complete primary circuit including the reactor and the turbine are placed in a confinement building which is little resistant to pressure.

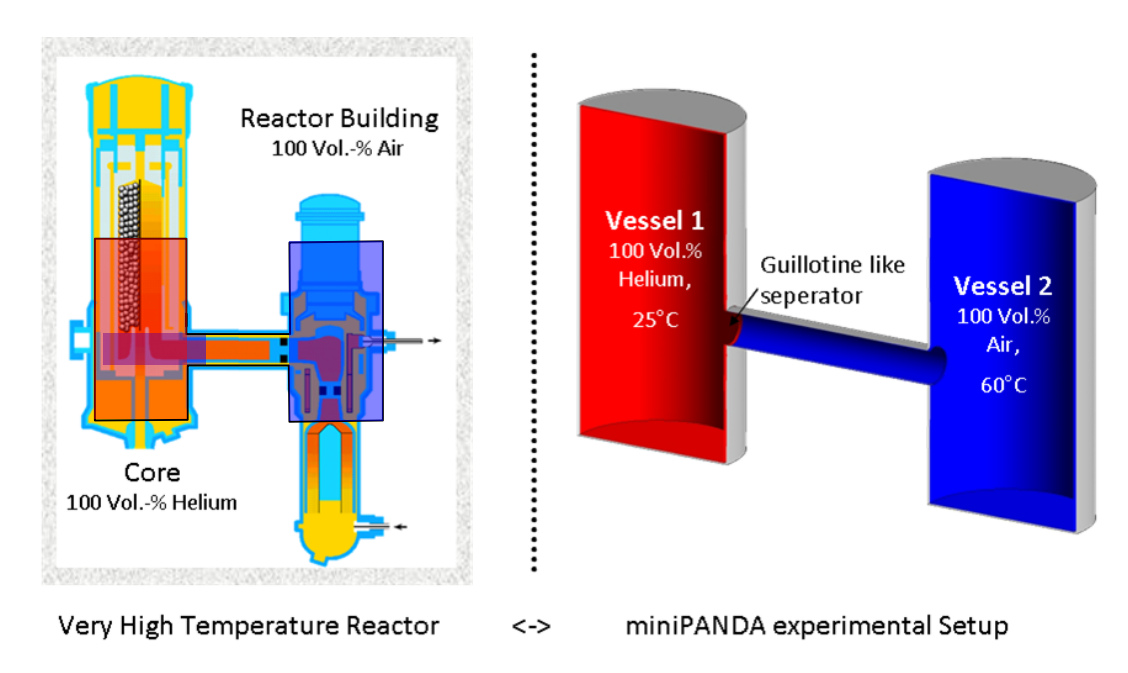


Figure 4: Counterparts of the MiniPanda facility in the VHT reactor.

A major possible accident scenario threatening the integrity of the reactor internals identified by the IAEA is the loss of cooling accident (LOCA) and the following air ingress scenario (Scherer and Gerwin 1993). This accident is initiated by a rupture in the primary circuit. Theoretically this break can happen at any position and with any shape at the primary circuit, however the rupture

of a small pipe like the connecting pipe between the core and the heat exchanger have the highest probability of occurrence (Chang 2009).

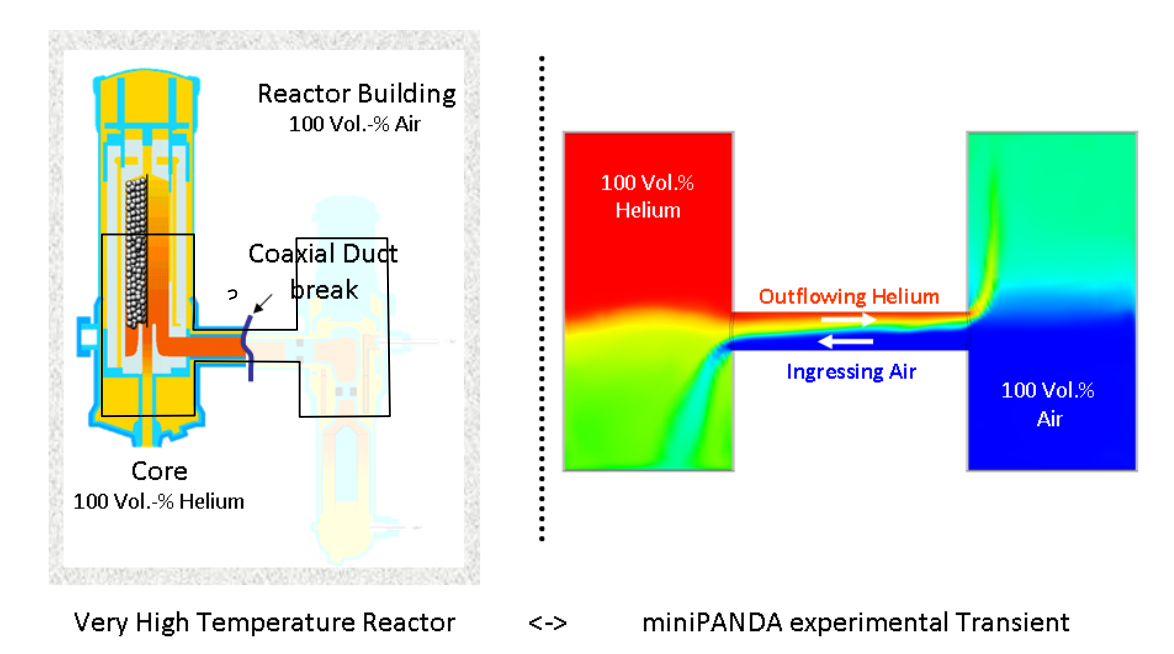


Figure 5: Course of the air ingress accident (left) and the analogies in the test facility (right).

Such an accident transient can be subdivided into four phases:

- 1) Blowdown: Caused by the overpressure within the primary circuit the helium flows into the confinement building. Due to the expansion the helium cools down.
- 2) Gravity driven air ingress: The residual heat increasing the helium temperature again and due to the increase of the volume helium is still pressed out of the reactor. Nevertheless at the break a gravity driven counter flow of helium and air occurs. The air is concentrated at the lower plenum.
- 3) Diffusion of Oxygen into Helium: On the basis of the density difference, the higher reactor core part is protected by the lighter helium. Anyway, oxygen diffuses into the helium layer.
- 4) Corrosion: When the oxygen reaches the hot graphite structure, such as the bottom reflector, corrosion happens and a natural convection driven flow transports more air into the core. The time between the rupture and begin of corrosion is called onset time. For safety analyses it is important to have a good prediction of the onset time.

During Nureth-13 another scenario, namely a break of a standpipe attached to the upper head was assumed, too (Jackson and Woods 2009), earlier assumed by (Hishida, Fumizawa et al. 1993). In contrary to the case of an assumed break of the main coolant line, then the density difference between air and helium would enhance the air ingress which could lead to a more rapid and severe accident evolution. An assumed break angle of 90° at the upper reactor head was found to result in the fastest air ingress according to that Fluent simulations.

## 3.2 Experiment description

In total 11 experiments were conducted within a test matrix varying the initial helium concentration in the helium vessel as well as the shape of the pipe connecting the "reactor vessel" (Vessel 1) initially filled with helium and the "containment vessel" (Vessel 2) initially filled with air. Repetition experiments proved the good repeatability of the experimental results.

Init. mol. helium fraction / 2122	20 % / 0.92	50 % / 0.63	100 % / 0.16
Straight connecting pipe	Exp6, Exp7, Exp8	Exp4, Exp5	Exp9, Exp10
Bent connecting pipe	Exp11	Exp12, Exp13	Exp14

Table 2: Test matrix for the air ingress experiments at MiniPanda.

In this context, Exp9 was chosen where 100% helium interacts with 100% air through a straight pipe. In the preparation phase of this experiment, the interconnecting pipe was blocked at the side of Vessel 1 (reactor vessel) by a metal sheet. On this side, a frame was installed, serving as a sliding guide for the metal sheet and holding two electro magnets that pulled the metal sheet against the front side of the IP end when activated. Vessel 2 (containment vessel) was heated for approximately three hours until the air of Vessel 2 and the connecting pipe (IP), as well as the walls of Vessel 2 and the IP reached the desired initial temperature of 60°C. Vessel 1 was filled with pure helium and remained unheated at room temperature of 25°C. Well controlled initial and boundary conditions were guaranteed by the homogeneous filling and conditioning of both vessels during the preconditioning phase and have been proved by the repeated test Exp 10. The temperature difference between the two gases served as a tracer to visualize the mixing process by means of the TMS and had no physical meaning to the investigated phenomena.

A sudden initiation of the transient process was achieved by switching off the magnets that held the blocking metal sheet in place. The metal sheet rapidly slid down by gravity like a French guillotine.

The main phenomena of the initiated air ingress are sketched in Figure 6 and can be summarized as follows:

- Air ingressed into the lower part of Vessel 1 (reactor vessel) and helium ingressed into the upper part of Vessel 2 (containment vessel). Partial mixing was taking place, clouds of different temperatures were still observed.
- A counter-current flow was set up in the IP with cold helium on top and hot air on the bottom.
- The volumes which were not affected by the ingressing plumes remained in their initial state.
- The downward air plume and the upward helium plume were detached from the wall. They were characterized by a local maximum/minimum in the cross-sectional temperature distribution and a local maximum in the short term standard deviation, i.e. temperature fluctuations. The temperature fluctuations measured at the plume-sensor-intersections indicated an oscillatory movement of the plumes. Anyway, the air plume penetrated further into Vessel 1 than the helium plume penetrated into Vessel 2.
- The cold wall of Vessel 1 cooled the gas mixture that was heated up by the hot ingressing air. The hot walls of Vessel 2 re-heated the gas mixture that was cooled down slightly by the cold incoming helium.

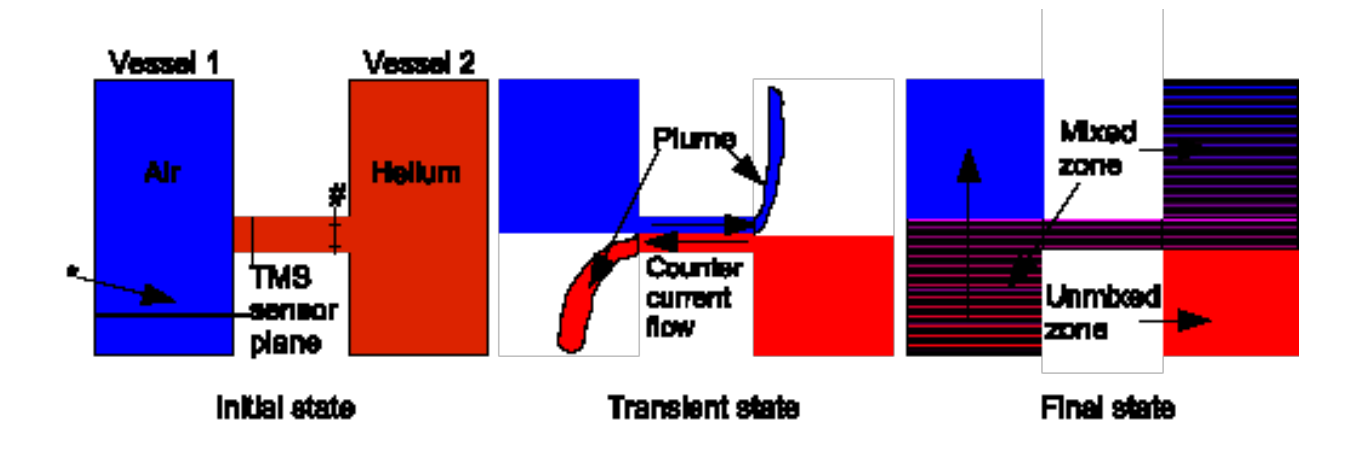


Figure 6: A sketch summarizing the characteristic key phenomena of the air ingress scenario transient (blue=helium, red=air) by way of an example. \* marks the position of the temperature and the air fraction measurement, # marks the positions of the anemometers.

The experiments' temperature and pressure did not match the conditions in the accident scenario. Since the experiment emulates the conditions after the blow-down (pressure equilibrium between reactor pressure vessel and containment at 1.3 bar and 290°C (Jühe 2005)), it was expected that the lower experimental pressure didn't change flow phenomena. The major driving force was buoyancy that is influenced by the gas composition and the gas temperature of reactor and containment side, respectively. As long as both gases are at the same pressure, the pressure does not effect the buoyancy and consequently not either the flow phenomena.

A possible influence on the buoyancy was identified by the temperature and gas composition mismatch. In fact, the density ratio was 0.12 in the scenario (pure air outside the reactor pressure vessel assumed (Jackson and Woods 2009) (different discharge scenarios result in high helium fractions at the containment side up to 80%) (Jühe 2005)) and 0.16 in the experiment, respectively. A series of experiments with several initial density ratios allows for an investigation and density-based scaling of the experiment.

The mismatch of fluid properties due to different temperatures in the experiment is negligible since they are superimposed by their turbulent counterparts (e.g. eddy viscosity, turbulent Schmidt-number). It can be stated that the main flow phenomena will qualitatively be the same as compared to the accident scenario and thus, the experiments data can be used for code validation.

# 3.3 Comparison

Two CFD-models, one based on ANSYS CFX13 (ANSYS, 2011), the other one on StarCCM+ (5.06.007) (CD-Adapco 2011), have been benchmarked to the MiniPanda Exp9. The modeling choices, boundary and initial conditions and numerical settings are compared in Table 3. In order to limit the influencing parameters, most settings have been aligned. However, settings differ especially regarding the applied turbulence model and wall treatment.

While within the StarCCM+ simulation the well-known realizable k-ε model is applied, the CFX model uses the new scale adaptive SAS-SST model. This model is based on a SST formulation for steady regions (e.g. boundary layers) and blends over to a scale resolving simulation in unsteady regions (ANSYS, 2011). The CFX model uses a low-Reynolds wall treatment and

considers conjugate heat transfer, while in StarCCM+ the model is simplified by a 2-layer wall function boundary condition and a prescribed wall temperature.

In order to limit the max Courant Number to a value of 2, the time steps are very short for the first 80 s. In this period the highest flow velocity occurs due to the high initial density difference. After the first 80 seconds the time steps are increased.

Figure 5 compares the applied grids. CFX uses a structured grid of the full facility, in StarCCM+ an unstructured polyhedral grid (base cell size of 3 cm) representing half of the facility and introducing a symmetry plane is applied.

Table 3: Summary of models, boundary and inital Conditions and numerics .

	StarCCM+	CFX 13	
<b>Equations solved:</b>			
Governing equations:	unsteady Reynolds Averaged	unsteady Reynolds Averaged	
	Navier Stokes (U-RANS)	Navier Stokes (U-RANS)	
	equations	equations	
	coupled energy, flow and		
	species		
Equation of state	ideal gas ("full buoyancy" model)		
Turbulence model	Realizable k-E +buoyancy	SAS-SST(incl. Buoyancy	
	effects production & dissipat		
Transport Properties	constant	constant	
<b>Boundary Conditions:</b>			
Inner Walls (thermal)	$T_{w,DW1}=22$ °C	Conjugate heat transfer	
	$T_{w,DW2}=60$ °C		
Inner Walls (flow)	two layer all y+ treatment	Low-Reynolds	
	Wall Functions		
Outer Walls (thermal)	None (solid heat conduction	heat conduction 5W/m <sup>2</sup> K; T <sub>env</sub> =298K	
	not simulated)		
Initialisation:			
Temperature	DW1: 298 K, IP: 321 K: DW2:333 K		
He-Concentration	DW1 (100vol%He), IP+DW2 (100vol% Air)		
Velocity	u,v,w=0 m/s (starts from rest)		
Numerics:			
Grid	3 cm base size, polyhedral	hexaedral 360°	
	180°-sym		
Spatial discretisation	2 <sup>nd</sup> order	2 <sup>nd</sup> order	
Temporal discretisation	2 <sup>nd</sup> order coupled implicit	2 <sup>nd</sup> order Euler backward	
Time steps	0.005 (180s), 0.02s (>80s)	0.005 (180s), 0.01s (>80s	
Convergence criteria	20 inner loops	RMS residuals <1e-4	

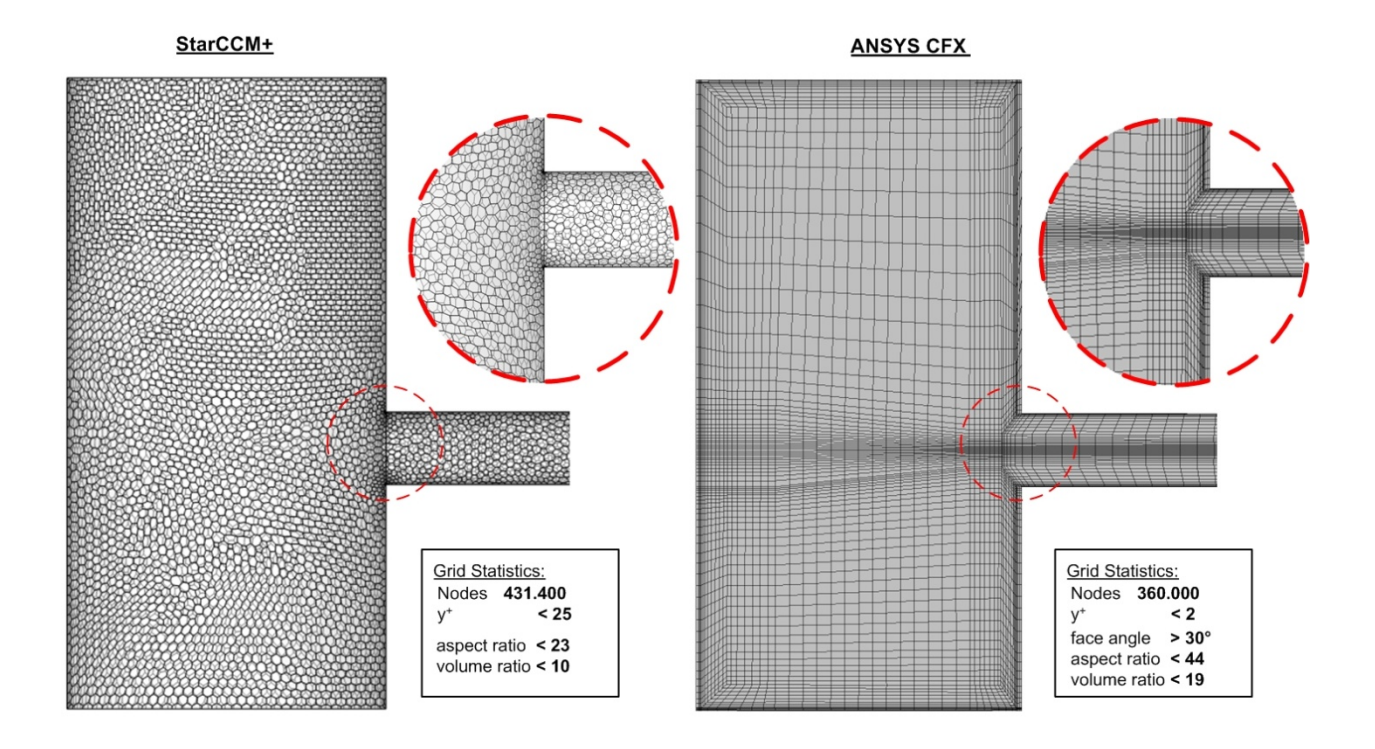


Figure 7: Mesh comparison between the automatically generated unstructured mesh generated with StarCCM+ and the manually blocked structured mesh used for CFX.

Following, the air ingress into the left vessel is investigated in detail considering the evolution of the molar air fraction and the temperature (as a marker for the air fraction) in the lower part of the Vessel 1 ("reactor vessel"). Further, the cross-sectional temperature and the vertical velocity distribution in the connecting pipe are compared in order to focus on the counter current flow.

Figure 8 displays the evolution of the molar air fraction and the temperature measured 0.414 m above the ground on the center axis of Vessel 1 (marked with a star). The results are in good agreement with each other and end up all in the same final value. The transient air fraction for t<100 s increase is slightly overestimated by CFX while it is slightly underestimated by StarCCM+.

The temperature measured (blue) at the same point displays first an increase until about 30 s what is due to the ingress of warm air. The warm air settled at the bottom of the vessel with a warm mixed zone on top. The fairly constant temperature between 40 and 70 s results from the fact that the ingressing air still went down below the sensor. After 70 s, the pile-up of the warm air reached the sensor level, thus resulting in an increase of temperature. Since the walls of Vessel 1 were cold, ingressed air cooled down and the overall temperature decreased as soon as the ingress finished after about 100 s. The cool-down process starts for StarCCM+ a little too early and proceeds too rapid, which can be explained with the simplified constant temperature boundary condition that neglects the slight heat-up of the vessel shell due to the hot air. In CFX, the wall was modeled together with an outer free convection boundary condition. The cool-down rate is overpredicted by CFX but the temperature ends up with a value close to the experimentally determined 28°C.

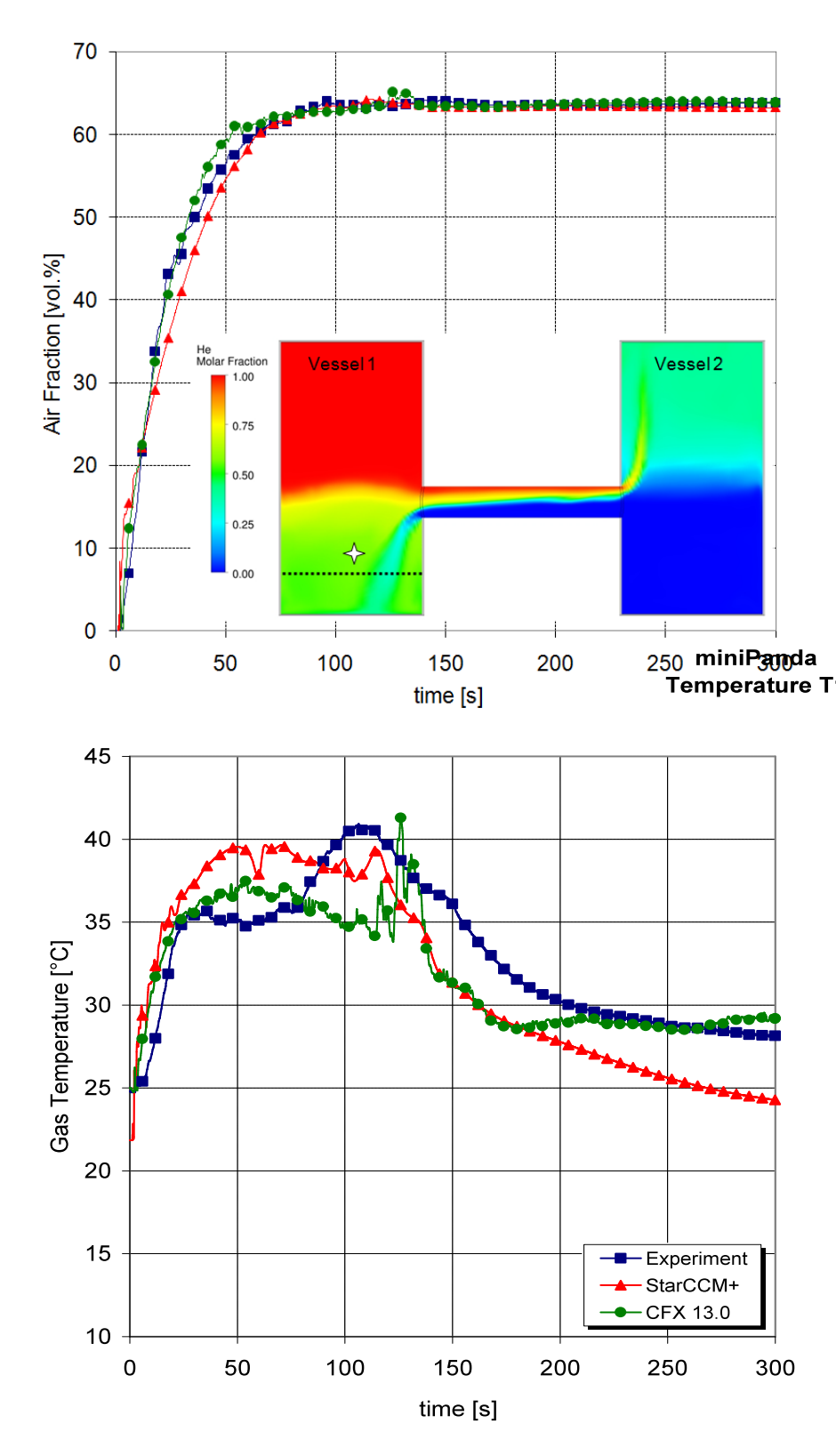


Figure 8: Comparison between experimental and analytical molar air fraction and temperature evolution in the lower part of Vessel 1 (marked with a star). Legend applies also to the upper graph.

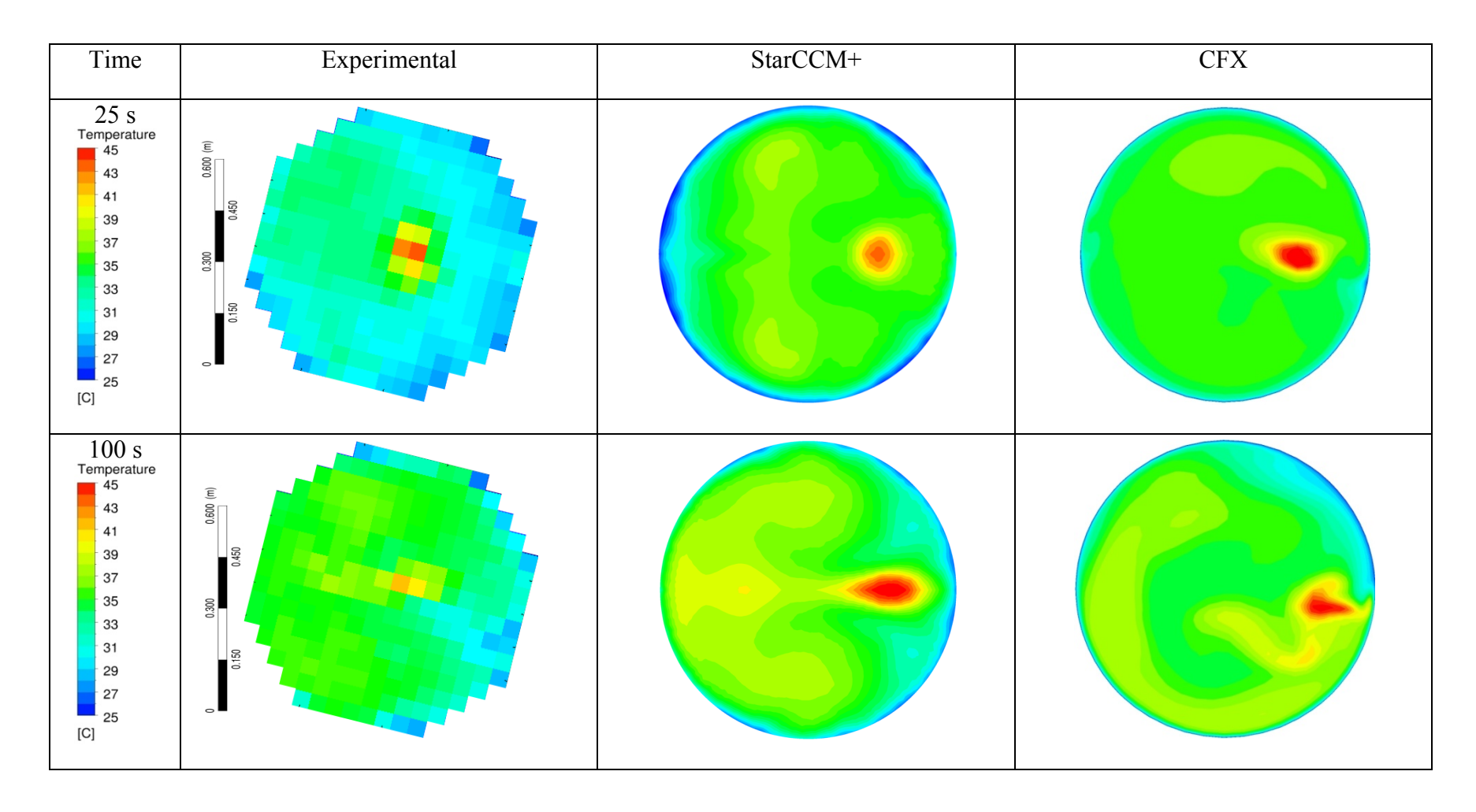


Figure 9: Comparison between experimental and analytical temperature distribution in the lower part of Vessel 1 (marked with a dotted line in Figure 8) after 25 and 100 s.

The cross-sectional temperature distribution at a level of 0.33 m above the bottom is compared in Figure 9. The jet position is indicated by the maximum temperature. The simulations predict the jet to fall down too close to the wall; the jet distance from the wall is tabulated in Table 1.

Time	Experimental	StarCCM+	CFX
25 s	0.40 m	0.25 m	0.25 m
100 s	0.44 m	0.22 m	0.17 m

Table 4: Jet distance from the right wall in 0.33 m altitude after 25 and 100 s.

The temperature distributions of the simulations after 25 s show a uniform, well mixed regime. In contrast, the experiment shows, as discussed before, that the mixing is less intense than predicted and that the hot air remains at the bottom, visible through the large cold (blue) area on the right side of the cross-section. After 100 s (see lower line in Figure 9), the air ingress is about turning into a diffusion driven regime. In fact, the experimental temperature distribution displays asymmetric 3D-character. The CFX solution also displays asymmetric temperature distributions in contrary to the StarCCM+ solution that was solved on half of the mesh, assuming 180° symmetry. The temperature maximum was found almost in the centre of the vessel. A similar behaviour is predicted by the StarCCM+ simulation.

In Figure 10 the velocities measured in the upper and lower part of the connecting pipe indicating the velocity of the ingressing air (from right to left, negative velocity) and the velocity of the outflowing helium, respectively. The results are in good agreement. Only the velocity of the outflowing helium is underestimated by StarCCM+ during the first 70 s of the experiment. This might be due to the coarser mesh inside the IP used for StarCCM+ compared to the refined mesh used for CFX which better resolves the vertical counter-current flow velocity gradient present in the pipe.

The temperature distributions from Figure 11, measured inside the IP (marked with a dotted line in Figure 10) indicate three areas: a warm one on the bottom of the IP (displayed in orange, ingressing air), the interface layer (green), where the mean velocity is about zero, and a cold area on top (outflowing helium). A comparison between the three plot shows, that the position and the width of the interface layer are well predicted within the spatial resolution (24 mm) of the TMS\_IP. The coarse mesh used for StarCCM+ leads to washed out gradients compared to the fine mesh used for CFX. Since a constant temperature boundary condition was applied for StarCCM+, the wall layer is heated up what can be seen as a "green" ring. The CFX solution provides a thermal stratification also in the air and in the helium flow area which cannot be seen in the experiment, where both, the air and the helium flows are well mixed.

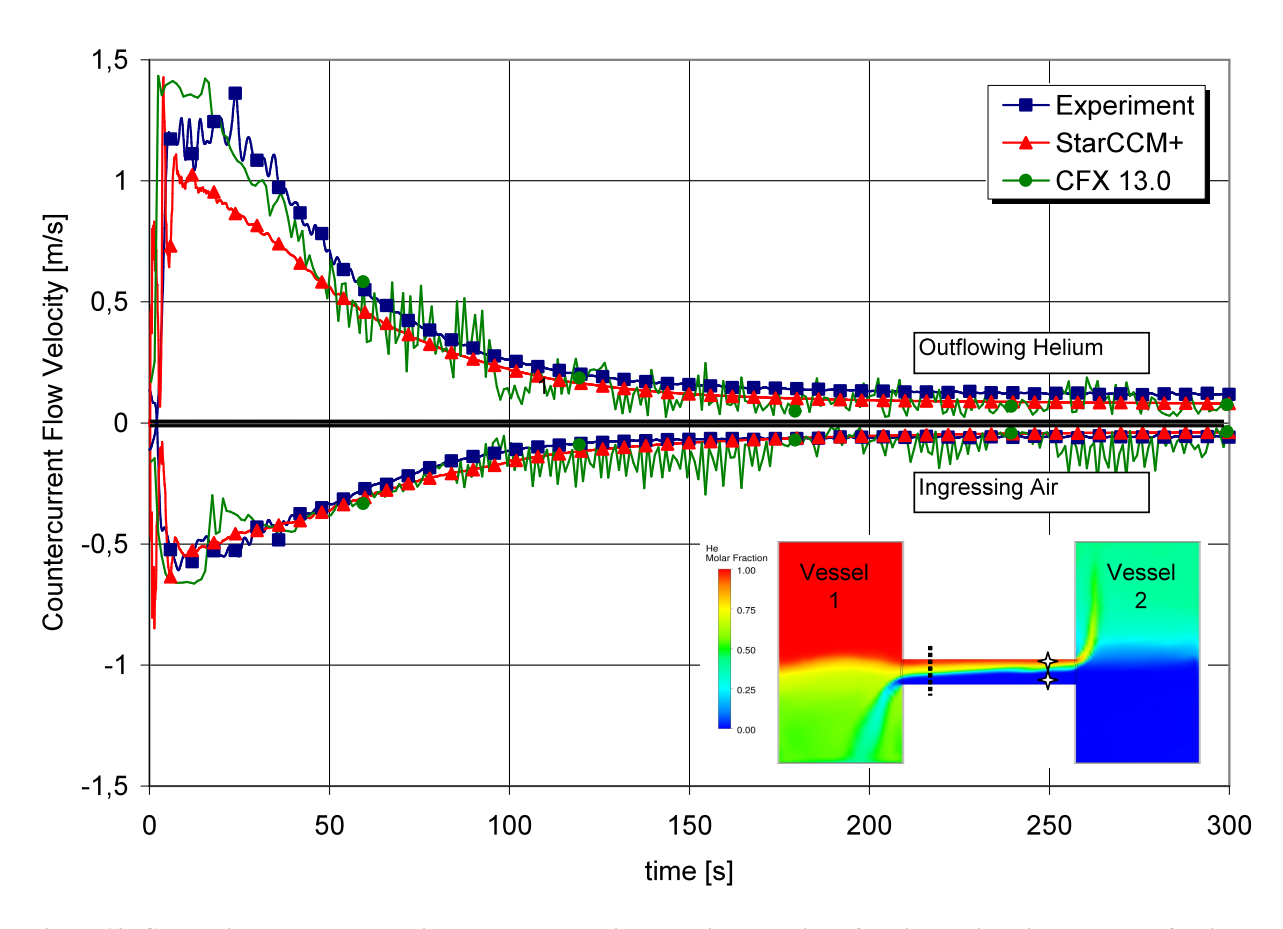


Figure 10: Comparison between experimental and analytical velocity evolution of the ingressing air and the outflowing helium in two levels of the IP (marked with a star)

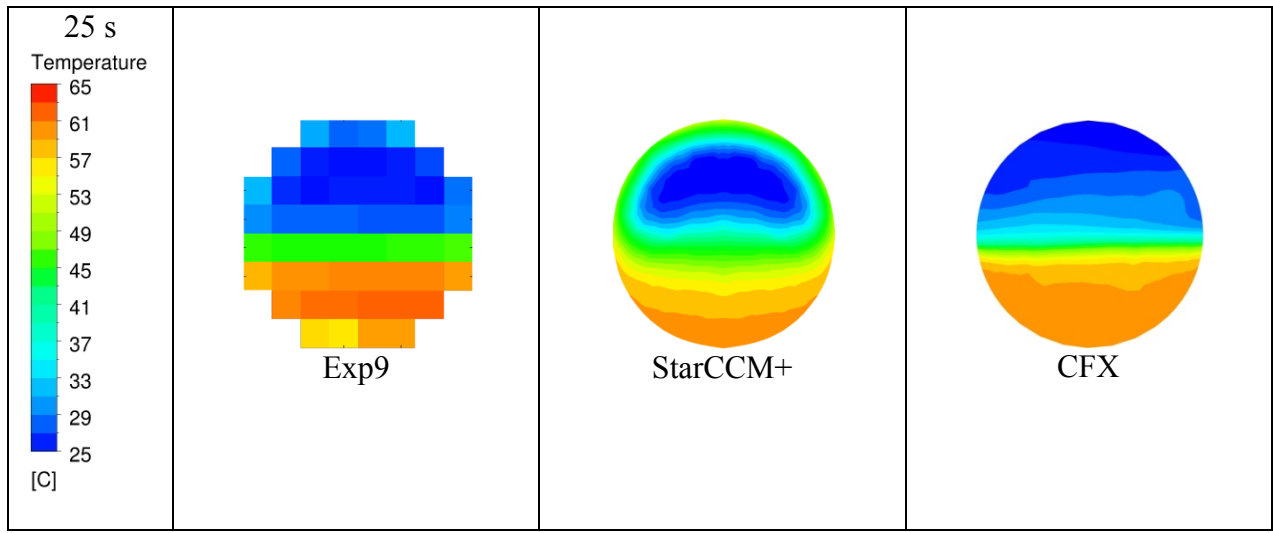


Figure 11: Comparison between experimental and analytical temperature distribution in the IP (marked with a dotted line in Figure 11) after 25 s.

## 4. Conclusions/Outlook

A new small (/smart-) scale facility was introduced, designed to provide high quality, CFD-grade data. The facility enables the application of novel instrumentation able to provide 2D temperature field data with a spatial resolution in the order of magnitude of the cell size used for CFD meshes.

The ingress of warm air into a helium filled vessel was investigated experimentally with well controlled initial and boundary conditions. The very good agreement of measured data among repetition experiments proved the high data quality.

Data obtained has been used to benchmark the commercial codes CFX13 and StarCCM+ 5.06. The codes are able to reproduce the field and point measurements in a qualitative way which implies on the one hand that the measured effects have been understood and on the other hand highlightens the quality of the experimental database. Nevertheless, small quantitative deviations are observed in terms of magnitude of temperature, velocity and temperature distribution and motivate a closer look to the modelling choices and especially on the numerical issues. Suspected reasons for the deviations are problems of the code with the turbulence model and the turbulent mixing in the diffusive environment and impulse interaction of the light helium and the heavy air. Further investigations, which have already started, will study the influence of grid and time step as well as turbulence modelling. In this context, MiniPanda offers due to its relatively small dimensions the possibility to calculate these parameters e.g. density differences in order to identify trends in the deviations and by this needs for model improvement.

The generell agreement between experimental and analytical data shows that the experiment has been understood and can be simulated in its basic characteristics and that the experimental data is free of side effects. The effects are displayed by the simulation. Remaining deviation resulted from the comparison of signal point evolutions in gradient environment or are found to be small in detailed quantities such as the plume position. The results are a motivation to continue modeling and model developmend and to use the whole test series for validation.

The subsequent test series in MiniPanda will deal with the erosion of a stratified helium layer due to a vertical jet from below in the context of containment safety. Helium will be used as a substitute gas for hydrogen which is produced after a severe accident with fuel rod cladding oxidation (see Nureth14, Log 442).

## 5. References

Allelein, H. J., K. Fischer, et al. (2007). "International Standard Problem ISP-47 on Containment Thermal-hydraulics." <u>NEA News 2007</u> **25.2**.

CD-Adapco (2011). StarCCM+ Version 5.06.007.

Chang (2009). <u>Thermal Hydraulics of the Very High Temperature Gas Cooled Reactor</u>. NURETH-13, Kanazawa, Japan.

Damsohn, M. and H. M. Prasser (2009). "High-speed liquid film sensor for two-phase flows with high spatial resolution based on electrical conductance." <u>Flow Measurement and Instrumentation</u> **20**(1): 1-14.

Dreier, J., D. Paladino, et al. (2008). <u>PANDA: a Large Scale Multi-Purpose, Test Facility for LWR Safety Research</u>. PHYSOR08, Interlaken, Switzerland.

EPCOS (2009). NTC Thermistors - General technical information, EPCOS AG.

Hishida, M., M. Fumizawa, et al. (1993). "Researches on air ingress accidents of the HTTR." <u>Nuclear Engineering and Design</u> **144**(2): 317-325.

Jackson, R. B. and B. G. Woods (2009). <u>CFD Modeling of Air Ingress into the Upper Plenum of Gas Reactor through Standpipe</u>. Nureth-13, Kanazawa City, Ishikawa Prefecture, Japan.

Jühe, S. H. (2005). Berechnung der Druckentlastung aus einem Leck im Heliumkreislauf eines Hochtemepraturreaktors sowie des Druckaufbaus und der Gasverteilung in den angrenzenden Räumen. Lehrstuhl für Reaktorsicherheit und -technik. Jülich, RWTH Aachen.

Kliem, S., T. Höhne, et al. "Experiments on slug mixing under natural circulation conditions at the ROCOM test facility using high-resolution measurement techniques and numerical modeling." <u>Nuclear Engineering and Design</u> **In Press, Corrected Proof**.

Melpignano, G. and D. Vles (2009). Development of a novel sensor for gas mixing experiments (semester project). Zürich, ETHZ-LKE.

NEA/CSNI (2008). Assessment of computational fluid dynamics (CFD) for nuclear reactor safety problems. <u>Nuclear Safety</u>. Issy-les-Moulineaux, France, OECD. **R(2007)13**.

Öztürk, O. C. (2010). Small Scale Experiment for the Comparison with An Air Ingress Scenario Simulation. <u>IET - Laboratory for Nuclear Energy Systems</u>. Zürich, ETHZ - Swiss Federal Institue of Technology. **Master**.

Prasser, H.-M. (2007). "Evolution of interfacial area concentration in a vertical air-water flow measured by wire-mesh sensors." <u>Nuclear Engineering and Design</u> **237**(15-17): 1608-1617.

Prasser, H. M., A. Böttger, et al. (1998). "A new electrode-mesh tomograph for gas-liquid flows." Flow Measurement and Instrumentation 9(2): 111-119.

Ritterath, M., U. Hampel, et al. (2008). Anordnung zur zweidimensionalen Messung der Temperaturverteilung in einem Messquerschnitt. DE 10 2007 019 925 A1, Germany.

Ritterath, M., H.-M. Prasser, et al. (2010). "New gas concentration measurement system for the PANDA containment test facility." Nuclear Engineering and Design **in press**.

Ritterath, M., P. Voser, et al. (2009). <u>Robust Thermal Flow Sensor for a Containment Test Facility</u>. IEEE Sensors, Christchurch, New Zealand, IEEE.

Scherer, W. and H. Gerwin (1993). "Scenarios of Hypothetical Water and Air Ingress in Small Modular HTGRs." IAEA TECDOC-784.

Silva, M. J. d., E. Schleicher, et al. (2009). Advanced wire-mesh sensor technology for fast flow imaging. <u>International Workshop on Imaging Systems and Techniques</u>. Shenzhen, China.

Smith, B. (2008). <u>Assessment of CFD for Nuclear Reactor Safety</u>. OECD/NEA & IAEA workshop Experiments and CFD Code applications to Nuclear Reactor Safety XCFD4NRS, Grenoble, France, NEA/CSNI/R(2009)12.

teletronic (2007). Wire mesh Sensor System SGITT 100 Manual. <u>SGITT 100 Manual</u>. Radeberg, Germany, teletronic Rossendorf GmbH **Version 1.2.0**, **Revision 1.0**.

Teschendorff, V. (2008). <u>The Role of CFD in NPP Safety</u>. XCFD4NRS, Grenoble, OECD-NEA & IAEA.

ANSYS (2011) "ANSYS CFX Version 13: Solver Theory", ANSYS inc., 2011

Smith, B. (2008) "Assessment of CFD for Nuclear Reactor Safety," Proc. OECD/NEA & IAEA workshop Experiments and CFD Code applications to Nuclear Reactor Safety XCFD4NRS, NEA/CSNI/R(2009)12, September 10th-12th 2008